energies

Article

Multi-Mode Damping Control Approach for the Optimal Resilience of Renewable-Rich Power Systems

Herlambang Setiadi [1,*], Nadarajah Mithulananthan [2], Rakibuzzaman Shah [3], Md. Rabiul Islam [4], Afef Fekih [5], Awan Uji Krismanto [6] and Muhammad Abdillah [7]

[1] Faculty of Advanced Technology and Multidiscipline, Campus C UNAIR Mulyorejo, Universitas Airlangga, Surabaya 60115, Indonesia
[2] School of Information Technology and Electrical Engineering, The University of Queensland, St. Lucia, QLD 4072, Australia; mithulan@itee.edu.au
[3] Centre for New Energy Transition Research (CfNETR), Federation University Australia, Mt. Helen, VIC 3353, Australia; m.shah@federation.edu.au
[4] School of Electrical, Computer and Telecommunications Engineering, University of Wollongong, Wollongong, NSW 2522, Australia; mrislam@uow.edu.au
[5] Department of Electrical and Computer Engineering, University of Louisiana at Lafayette, Lafayette, LA 70504-3890, USA; afef.fekih@louisiana.edu
[6] Electrical Engineering Department, Institut Teknologi Nasional Malang, Malang 65145, Indonesia; awan_uji_krismanto@lecturer.itn.ac.id
[7] Electrical Engineering Department, Universitas Pertamina, Jakarta 12220, Indonesia; m.abdillah@universitaspertamina.ac.id
* Correspondence: h.setiadi@ftmm.unair.ac.id

Abstract: The integration of power-electronics-based power plants is developing significantly due to the proliferation of renewable energy sources. Although this type of power plant could positively affect society in terms of clean and sustainable energy, it also brings adverse effects, especially with the stability of the power system. The lack of inertia and different dynamic characteristics are the main issues associated with power-electronics-based power plants that could affect the oscillatory behaviour of the power system. Hence, it is important to design a comprehensive damping controller to damp oscillations due to the integration of a power-electronics-based power plant. This paper proposes a damping method for enhancing the oscillatory stability performance of power systems with high penetration of renewable energy systems. A resilient wide-area multimodal controller is proposed and used in conjunction with a battery energy storage system (BESS) to enhance the damping of critical modes. The proposed control also addresses resiliency issues associated with control signals and controllers. The optimal tuning of the control parameters for this proposed controller is challenging. Hence, the firefly algorithm was considered to be the optimisation method to design the wide-area multimodal controllers for BESS, wind, and photovoltaic (PV) systems. The performance of the proposed approach was assessed using a modified version of the Java Indonesian power system under various operating conditions. Both eigenvalue analysis and time-domain simulations are considered in the analysis. A comparison with other well-known metaheuristic methods was also carried out to show the proposed method's efficacy. Obtained results confirmed the superior performance of the proposed approach in enhancing the small-signal stability of renewable-rich power systems. They also revealed that the proposed multimodal controller could enhance the penetration of renewable energy sources in the Javan power system by up to 50%.

Keywords: clean energy technology; extreme learning machine; fruit fly optimisation; photovoltaic; renewable energy; wind power plant

Citation: Setiadi, H.; Mithulananthan, N.; Shah, R.; Islam, M.R.; Fekih, A.; Krismanto, A.U.; Abdillah, M. Multi-Mode Damping Control Approach for the Optimal Resilience of Renewable-Rich Power Systems. *Energies* **2022**, *15*, 2972. https://doi.org/10.3390/en15092972

Academic Editor: Miguel Castilla

Received: 18 March 2022
Accepted: 18 April 2022
Published: 19 April 2022

1. Introduction

Power electronics devices are widely used in renewable energy systems (RESs) such as wind and PV. The implementation of power electronics devices is anticipated to further increase due to the high penetration of RESs, battery energy storage systems (BESS), and high and medium-voltage DC interconnectors in future power grids. Moreover, the increased penetration of power-electronics-based loads (i.e., smart and fast-charging EV) into the grid is expected to lead to a rise in power electronics devices on the demand side. However, power electronics and their controllers could bring new challenges in maintaining power system stability, especially small-signal stability [1]. The low- and no-inertia characteristics of a power-electronics-based system may create low-frequency oscillatory issues in the system. Moreover, the stochastic nature of RESs output could render the control of power-electronics-based generation further challenging [2,3].

As reported in [4], the integration of large-scale PV plants could affect oscillatory or small-signal stability due to the distinct dynamic characteristics and reverse power flow in the system. In that paper, it was observed that the damping ratio of the electromechanical (EM) mode changed with the large-scale penetration of PVs. The impact of wind power plant penetration on the oscillatory stability of the grid was reported in [5]. That study showed that the penetration of wind power plants may bring both positive and negative influences on the oscillatory stability of power systems. It also found [5] that the integration of wind power could either influence the power system's low-frequency oscillation modes or contribute to new low-frequency oscillation modes. The researchers in [6] investigated the effect of the intermittent power output of renewable power plants on the system's oscillatory stability. Two different case studies are considered in this paper. The uncertainty of the wind power system was modelled with stochastic operating conditions. Eigenvalue, damping-performance, and participation-factor analyses are used to investigate the impact of stochastic wind outputs on power systems. Uncertainty in the power output of wind could adversely affect the oscillatory stability of the system. The influence of stochastic PV power on oscillatory conditions was reported in [7]. PV generation was modelled as a two-stage PV consisting of boost converter and MPPT control. DC link capacitor can act as a buffer between boost converter and inverter. The inverter is used as a link between PV generation and the grid. Two case studies were considered in this paper. The first case study uses two-area power systems, while the second considers the IEEE 39-bus system. Both time-domain simulations and damping performance assessments were utilised to investigate the impact of the uncertain power output of PV generation. Simulation results showed that the stochastic PV output could have an adverse effect on the oscillatory stability of the power system. The research above showed that, due to the integration of renewable power plants, the damping performance of the power system is decreased. Hence, it is important to add power oscillation damping to enhance the power system's damping.

Research efforts were undertaken to enhance the damping performance of the power system. The authors in [8] proposed the application of a multiband power oscillation damping controller for SVC. The proposed power oscillation damping is based on the PSS4B model. This damping controller is added as the additional controller of SVC. A two-area eleven-bus power system was used as the test system. Simulation results showed that the proposed method could enhance the damping performance of all electromechanical modes in two-area power systems. Research in [9] was devoted to enhancing the damping performance of the power system by using a modified power system stabiliser. This includes a controller with a combination of a power system stabiliser and a PID controller. A single-machine infinite bus was used as the test system in [9]. Simulation results showed that the proposed method could enhance the dynamic performance of a single-machine infinite bus over a broad range of operating conditions. The application of a multiband power system stabiliser to enhance the damping performance of the power system was reported in [10]. Analysis was conducted on a single-machine infinite bus and practical South-Southern Brazilian power system. The Newton–Raphson method was used to design the power system stabiliser. Simulation results showed that the dynamic performance of the single-machine infinite bus and the South-Southern Brazilian power system could be significantly enhanced. However, problems such as uncertainty, lack of inertia, and different dynamic characteristics were not considered in the previously mentioned research efforts. Hence, it is essential to add additional devices to address these issues. Many researchers and utilities considered BESS to manage the low inertia and power fluctuations of the RESs.

Several research efforts were also undertaken to use BESS to overcome the adverse effects of renewable generations on power system low-frequency oscillations. The work reported in [11] showed the impact of battery energy storage systems on low-frequency oscillation. The IEEE 68-bus is used as the test system to investigate the impact of the battery energy storage system on low-frequency oscillation. The test system was modified by adding a renewable power plant in buses 40, 49, and 50. Simulation results show that BESS can enhance the damping performance of the weak modes. The research in [12] was devoted to analysing the low-frequency oscillation enhancement using a battery energy storage system in the wind network with high penetrations of wind generations. It was observed that the battery energy storage could enhance the dynamic performance of power systems considering wind power plants. Although the BESS could enhance the system's dynamic performance with renewable energy, the influence of BESS on oscillatory stability may not be noteworthy. Hence, it is essential to add more controllers such as the power oscillation damping (POD) controller at BESS to enhance the damping performance of the critical modes.

The authors in [13] proposed a method for enhancing the damping performance of power systems by using POD in the energy storage system. An AC/DC microgrid was used as the test system. Dynamic loads such as induction motors are also considered. Nonlinear dynamic simulations with a wide range of disturbances and different operating conditions of the induction motor were performed to investigate the efficacy of the proposed controller method. Simulation results showed that the oscillatory condition of the AC/DC microgrid was improved when the proposed method was added to the system. The application of POD in power systems with renewable generations and BESS is reported in [14]. Analysis was conducted in the Indonesian Java power grid (i.e., a three-area power system). The POD was designed to be resilient to communication failures. Simulation results showed that the damping performance of the critical modes could be enhanced by adding PODs to the excitation system. The POD could also be designed to be resilient to communication failures. However, the implication of a control failure on the overall dynamic performance of the system was ignored. Moreover, the implication of synchronous generation replacement with such a control function was overlooked in [14].

Hence, it is essential to design a controller that can tackle both communication and controller failures. The researchers in [15] proposed a new control method called resilient wide-area multimodal controller (MMC). The controller was again added to generator excitation systems. Simulation results showed that the proposed controller could minimise the effects of both communication and controller failures. However, with the increasing penetration of renewable energy sources, these synchronous generators with auxiliary controls would be replaced with RESs in the future. Therefore, it is important to implement such controllers in renewable energy systems and BESS. A bat-algorithm-based multimodal controller was proposed in [15]. Obtained results confirmed the ability of the proposed approach to enhance the damping of the interarea mode. However, the bat-algorithm-based MMC is computationally expensive, and the impact of the controller on the internal dynamics of RESs and BESS was overlooked in that paper. Hence, designing an MMC that is less computationally expensive is essential.

Most recently, the FA was used in power system applications, including the tuning of the controller, which showed the suitability of FA in a power system application [16–19]. However, neither of these works considered the MMC for RESs and BESS, and the comprehensive comparison of various control methods.

We designed a robust low-computational-cost MMC for BESS and RESs. The firefly algorithm (FA) was selected for such a controller design. In addition, the impact of various control designs on the internal dynamics of RESs and BESS is investigated and reported in this paper.

The main contributions of this paper are as follows:

- Designing a multimodal controller that is resilient to signal loss and controller failure using the FA algorithm.
- Designing a damping controller for PV, wind, and BESS that is free from interaction with the internal dynamics of the system.
- Assessing the realistic representative system's low-frequency performance and identifying the penetration limit increment with the proposed control.

The rest of the paper is organised as follows. A modelling overview of renewable generation and battery energy storage systems is provided in Section 2. The control design is synthesised in Section 3. The results and discussion of this work are presented in Section 4. Some concluding remarks are lastly given in Section 5.

2. Modelling

2.1. Wind Power System

The permanent-magnet synchronous-generator-based full converter wind generation system represents the wind power system (WPS) in this work. The wind power system consists of the dynamic representation of a permanent-magnet synchronous generator, wind turbine, rotor, and grid-side converter including the associated controllers. The differential–algebraic equations for simulation studies represent the dynamic model of the wind energy system [20,21].

The generator-side AC/DC converter incorporates outer and inner control loops. The outer control loops measure the terminal and DC link voltages, and compares those measured values to their corresponding reference values. Errors are then controlled using conventional PI controllers to derive the reference values of d and q currents. By considering β_{dgen} and β_{qgen} as auxiliary state variables of the outer control loop of the generator-side converter, state equations of the controller can be represented by [22].

$$\frac{d\beta_{dgen}}{dt} = v_{dcref} - v_{dc}, \frac{d\beta_{qgen}}{dt} = v_{gen\_ref} - v_{gen} \tag{1}$$

Reference currents of the generator-side converter are given by

$$i_{dgen\_ref} = K_{i21}\beta_{dgen} + K_{p21}v_{dcref} - K_{p21}v_{dc} \tag{2}$$

$$i_{qgen\_ref} = K_{i11}\beta_{qgen} + K_{p11}v_{gen\_ref} - K_{p11}v_{gen} \tag{3}$$

Output variables from the outer control loop are then applied to the inner current control loop as reference values and compared with the actual values of the generator currents $\left(i_{dgen}, i_{qgen}\right)$. Auxiliary state variables of γ_{dgen} and γ_{qgen} are required to express the state equation(s) of the inner current controller(s) as follows:

$$\frac{d\gamma_{dgen}}{dt} = i_{dgen\_ref} - i_{dgen}, \frac{d\gamma_{qgen}}{dt} = i_{qgen\_ref} - i_{qgen} \tag{4}$$

A similar algorithm is implemented to the current control loop to determine the modulation indices $\left(m^*_{dgen}, m^*_{qgen}\right)$ for the generator-side converter. These modulation indices are then employed as control variables for the PWM switching scheme of the converter. Algebraic equations of the reference signals corresponding to the modulation indices for the generator-side converter are given by the following equations [22]:

$$m^*_{dgen} = K_{i41}\gamma_{dgen} + K_{p41}i_{dgen\_ref} - K_{p41}i_{dgen} \tag{5}$$

$$m_{qgen}^{*} = K_{i31}\gamma_{qgen} + K_{p31}i_{qgen\_ref} - K_{p31}i_{qgen} \tag{6}$$

Like the generator-side control, the grid-side inverter control of WPS consists of outer and inner control loops. Calculated active and reactive power reference values in the outer control loop are compared to the measured active and reactive output power. The state equation of the grid-side outer control loop can be derived by considering β_{dgrid} and β_{qgrid} as auxiliary state variables using (7).

$$\frac{d\beta_{dgrid}}{dt} = P_{ref} - P, \frac{d\beta_{qgrid}}{dt} = Q_{ref} - Q \tag{7}$$

Obtained errors from outer control loops are then regulated by PI controllers, yielding the reference values for the inner current control loops as follows.

$$i_{dgrid\_ref} = K_{i22}\beta_{dgrid} + K_{p22}P_{ref} - K_{p22}P \tag{8}$$

$$i_{qgrid\_ref} = K_{i12}\beta_{qgrid} + K_{p12}Q_{ref} - K_{p12}Q \tag{9}$$

The inner current controller loops generate the modulation indices $\left(m_{dgrid}^{*}, m_{qgrid}^{*}\right)$ for providing the switching signal for the grid-side inverter. Auxiliary state variables of γ_{dgrid} and γ_{qgrid} are required to express the state equations of the inner current controller loops as follows:

$$\frac{d\gamma_{dgrid}}{dt} = i_{dgrid\_ref} - i_{od}, \frac{d\gamma_{qgrid}}{dt} = i_{qgrid\_ref} - i_{oq} \tag{10}$$

Reference signals corresponding to the modulation indices for the grid-side inverter are given by [22].

$$m_{qgrid}^{*} = K_{i32}\gamma_{qgrid} + K_{p32}i_{qgrid\_ref} - K_{p32}i_{oq} \tag{11}$$

$$m_{dgrid}^{*} = K_{i42}\gamma_{dgrid} + K_{p42}i_{dgrid\_ref} - K_{p42}i_{od} \tag{12}$$

2.2. PV Power System

The North American Electric Reliability Corporation (NERC) and Western American Electricity Coordination Council (WECC) developed a model of transmission-level PV that is suitable for stability studies in the electromechanical timeframe [23]. The dynamic model of the PV plant developed by NERC and WECC was later adopted in several state-of-the-art power system simulation environments, and consists of the converter and associated controllers [24,25]. The converter is represented by a set of first-order transfer function models [24]. The converter controller consists of PI controllers and current limiters. The dynamics associated with the DC link capacitor are not considered in this model due to the faster time step of the DC link compared to the electromechanical timeframe. The dynamics associated with the maximal power tracking are also ignored in this model due to the different time steps compared to the electromechanical oscillation. Moreover, the PV system was assumed to be operated around the maximal power point [23]. Figure 1 shows the dynamic model of a PV plant with a multimodal controller (considered in this paper). Detailed model and mathematical representation of PV plant dynamic model are presented in [26]. The PV's active power and voltage control are represented in (13) and (14).

$$I_{dref} = P_{PV}(G, T.x) \tag{13}$$

$$\frac{V}{V_{reff}} = \frac{X_s(k_p s + k_i)}{s + X_s(k_p s + k_i)} \tag{14}$$

where G represents irradiance, T is temperature, x is PV system parameters, P_{PV} is the power order from PV panel, I_{dref} is the d-axis reference current, V is terminal voltage, V_{reff} is reference voltage, X_s represents filter reactance, and k_p and k_i are the PI control parameters.

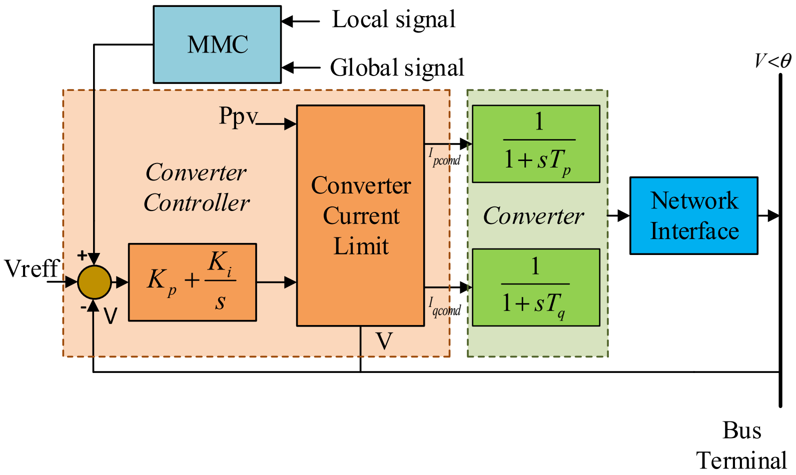

Figure 1. PV plant with multimodal controller.

The multimodal controller was integrated into the reactive power control block. In general, oscillation damping is related to the system's active power. Therefore, the modulation of active power is used for POD design. However, due to the stochastic behaviour of the PV system, the reactive power modulation was considered in this paper to dampen the oscillation of critical modes [23].

2.3. Battery Energy Storage System

This paper considers a modified version of the battery energy storage system (BESS) studied in [27]. This model consisted of a three-phase transformer, AC to DC converter, active and reactive power controllers, and battery dynamics. Figure 2 shows the dynamic model of the BESS with the multimodal controller. The multimodal controller could be implemented at the firing angle of the converter. Therefore, the BESS could modulate the required active and reactive power to the grid. Different battery energy storage system models can be used for electromechanical simulations [28]. However, the fifth-order battery model is considered for this study [27].

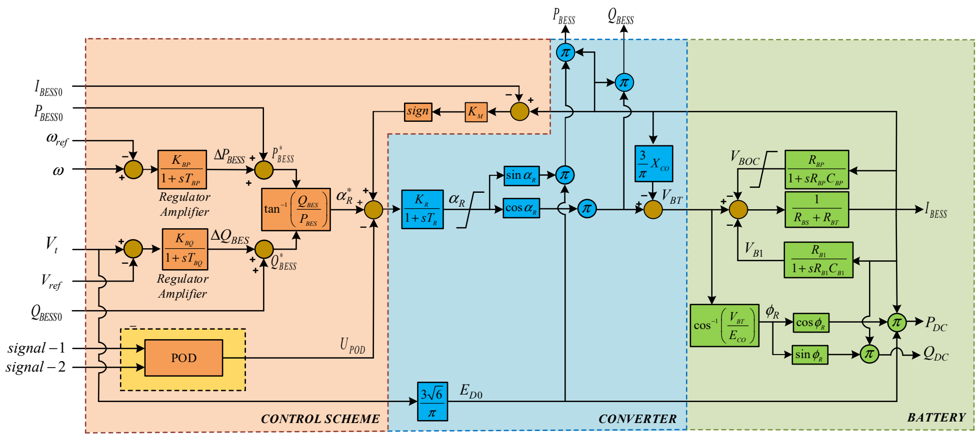

Figure 2. Dynamic model of BESS.

The BESS consisted of a second-order model of battery cells, a first-order model of converter dynamic, and a second-order model of active and reactive power control. The active and reactive power controller of BESS can be expressed as (15) and (16) [27]:

$$\Delta P_{BES} = \frac{k_{BP}}{1 + sT_{BP}} \Delta\omega \tag{15}$$

$$\Delta Q_{BES} = \frac{k_{BQ}}{1 + sT_{BQ}} \Delta V_t \tag{16}$$

In (15) and (16), K_{BP} and T_{BP} are the control loop gain and rotor speed measurement device time constant, respectively. K_{BQ} and T_{BQ} are the control loop gain and terminal voltage measurement device time constant. The converter dynamic can be obtained using (17) and (18) [27].

$$\alpha_R = \frac{k_R}{1 + sT_R} (\alpha_R^* + k_M \Delta I_{BES}) \tag{17}$$

$$\alpha_R^* = \tan^{-1}\left(\frac{Q_{BES}^*}{P_{BES}^*}\right) \tag{18}$$

In (17) and (18), K_R and T_R are the converter loop gain and the firing angle time delay constant. K_M and I_{BESS} are used to stabilise the BESS under constant current operation, so that BESS can release more power from batteries. Moreover, P_{BES}^* and Q_{BES}^* are active and reactive power output of converter controller. Furthermore, the dynamic model of battery cells can be described using (19) and (20) [27].

$$V_{BOC} = \frac{R_{BP}}{1 + sR_{BP}C_{BP}} I_{BES} \tag{19}$$

$$V_{B1} = \frac{R_{B1}}{1 + sR_{B1}C_{B1}} I_{BES} \tag{20}$$

In (19) and (20), R_{BP} and C_{BP} are used to describe the self-discharging of a battery. R_{B1} and C_{B1} represent energy and voltage during charging and discharging, respectively. Moreover, V_{BOC} and V_{B1} are the battery open-circuit voltage and battery voltage, respectively [27].

3. Method

3.1. Multimodal Controller

The concept of the multimodal controller is to design multiple controllers to enhance the damping of specific weak modes. In this concept, when one of the controllers fails, the other controller can work as a backup. Furthermore, the structure of this controller is multi-input multioutput (MIMO). Hence, this controller is also resilient to communication failures [15]. Figure 3 shows the multimodal controller (MMC) structure used in this paper.

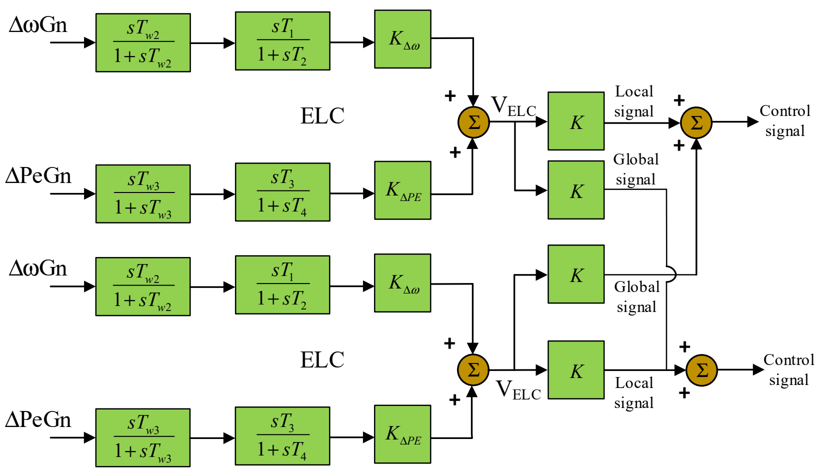

Figure 3. Multimodal control structure.

As depicted in Figure 3, the MMC consists of the gain constant and the external linear controller (ELC). The input of ELC is the rotor speed and electrical power of the generator that contributes to the weak modes. Moreover, inputs of MMC are the combination of ELC outputs scaled by the gain constant. Washout filters are used in each channel. The output of the washout filters is fed into the lead-lag block as given in Figure 3. The outputs of

MMC are the control signals to the BESS, wind, and PV power plant controller, as depicted in Section 2. To render the controller is more realistic, it is essential to add time delay representation to the controller.

3.2. Fruit Fly Optimisation

Two steps are used here to simulate sending- and receiving-end signal latency. To capture the dynamic behaviour of the time delay in the simulation, Padé approximation was used. The mathematical representation of the time delay based on Padé approximation can be described as [29]:

$$e^{-sTd} = \frac{1 - K_1 s + K_2 s^2 + \ldots \pm K_n s^n}{1 + K_1 s + K_2 s^2 + \ldots \pm K_n s^n} \tag{21}$$

In (21), the constant coefficient and the order of approximation can be described by $K_1, K_2, \ldots, K_n$, and n. The responses of the first- and second-order time delay model are similar. Hence, in this paper, the first-order time delay represents communication delay. In addition, receiving and sending end-time delays are considered. Local and global time delays of 100 and 700 ms, respectively, were considered. Furthermore, to obtain the best parameters of the MCC, FA was used as the optimisation method.

3.3. Firefly Algorithm

The firefly algorithm (FA) was inspired by the flashing activity of fireflies. This flashing behaviour acts as a signal to attract other fireflies [30]. This algorithm was first introduced by Xin She Yang [30]. There are three important rules and considerations for modelling the FA:

- Fireflies should be attached to others fireflies regardless of their sex.
- Attractiveness should be proportional to the brightness of the fireflies.
- The objective function can be determined by the brightness of the firefly.

In this research, the degree of light intensity influenced the attractiveness of the fireflies. The degree of light intensity of the x firefly can be described as in (22) [31].

$$I(x) = f(x) \tag{22}$$

In (19), the objective function and light intensity of fireflies are indicated by $f(x)$ and I, respectively. Furthermore, the attractiveness coefficient related to light intensity is indicated by β. This attractiveness coefficient is seen and assessed by other fireflies. Therefore, the distance between fireflies significantly influences the attractiveness coefficient. Furthermore, light intensity decreases due to the air factor (γ). In this paper, the air factor represents the condition of the air at a particular time. The air factor was modelled as a constant value for this work. Hence, the attractiveness function can be mathematically represented as (23) [31].

$$\beta(r) = \beta_0 \times exp(-\gamma r^m), (m \geq 1) \tag{23}$$

The distance between fireflies can be determined when all fireflies are randomly dispersed in the Cartesian diagram. The mathematical representation of the distance between different fireflies can be obtained as given in (24), where r_{ij} is the distance between fireflies i and j.

$$r_{ij} = \sqrt{\left(x_i - x_j\right)^2 + \left(y_i - y_j\right)^2} \tag{24}$$

In (24), the initial position of fireflies at location x and variables with values in the range of 0 to 1 are x_i and α. Equation (25) describes how to formulate the position of each firefly in a particular condition.

$$\begin{aligned} x_i &= x_i + \beta_0 \times exp\left(-\gamma r_{ij}^2\right) * \left(x_j - x_i\right) + \alpha \times \left(rand - \tfrac{1}{2}\right) x_i \\ &= x_i + \beta_0 \times exp\left(-\gamma r_{ij}^2\right) \times \left(x_j - x_i\right) + \alpha \times \left(rand - \tfrac{1}{2}\right) \end{aligned} \tag{25}$$

3.4. Implementation of FA

In this paper, FA was used as the optimisation method to design wide-area multimodal controllers for BESS, wind, and PV plants, since it is expected that conventional generators will be replaced by these sources. The FA was chosen as the optimisation method because FA can provide a simple code with optimal and faster results compared to other algorithms. A multiobjective function was used in this paper. The objective function of FA can be described as in (26).

$$Objective = min(aZ_1 + bZ_2 + cZ_3) \tag{26}$$

In (26), Z1, Z2, and Z3 are the mathematical equations that are later expressed in (27)–(29). The real parts of the i-th mode and the desired mode location are described by σ_i and σ_0. Furthermore, the damping value of the i-th eigenvalue and the desired damping value are presented as ξ_i and ξ_0. Moreover, the oscillatory condition of generator rotor speed, MMC parameters, and the timeframe for simulations are described by $\Delta\omega(t,X)$, X, and t_1. Weighting factors (i.e., a, b, c) vary from 0 to 1.

$$Z_1 = \sum_{\sigma_0 \geq \sigma_i} [\sigma_0 - \sigma_i]^2 \tag{27}$$

$$Z_2 = \sum_{\xi_0 \leq \xi_i} [\xi_0 - \xi_i]^2 \tag{28}$$

$$Z_3 = \sum \int_0^{t_1} t|\Delta\omega(t, X)|dt \tag{29}$$

Subject to

$$\begin{gathered} 10 \leq T_{W2}, T_{W3} \leq 20 \\ 0.05 \leq T_1 \leq 0.1 \\ 0.02 \leq T_2 \leq 0.1 \\ 0.03 \leq T_3 \leq 0.1 \\ 0.01 \leq T_4 \leq 0.1 \\ 5 \leq K_{\Delta\omega n} \leq 20 \\ 1 \leq K_{\Delta pen} \leq 2 \\ 50 \leq K_n \leq 100 \end{gathered} \tag{30}$$

Parameter bounds were selected on the basis of the IEEE recommendation standard. The concept applied here was to use the stochastic approach to determine the parameters of MMC. MMC parameters are explained in Figure 3. Upper and lower limits of parameters for MMC are given in (30). The simple pseudocode of the stochastic approach for tuning MMC parameters using FA is given in Appendix A.

4. Results and Discussion

To assess the performance of the proposed approach, we implemented it in a realistic representation of the 500 kV Java Indonesian electric grid (Figure 4). The machine parameters and the power flow were taken from a realistic representation of the Java, Indonesia electric grid. This grid is expected to be composed of 60% conventional and 40% renewable generators [32] by 2030. Therefore, to reflect this future generation mix, the synchronous generator at bus 4 was replaced by a large-scale transmission level PV plant of 300 MW capacity. An aggregated wind farm of identical size was integrated into bus 26. In addition, an aggregated wind farm of identical size was integrated into bus 26. Furthermore, a 100 MW BESS was added to bus 9 in area 2, as shown in Figure 4. All renewable power generation plants in this studied system were assumed to be operated at the maximal power point. Table 1 shows the EM modes of the modified Java Indonesian electric grid. The system consists of six local and one interarea modes. Among the identified EM modes, the interarea mode and one of the local modes (local mode 2) demonstrated lower damping (lower damping ratio than the industry standards, i.e., 0.05). From the initial participation factor analyses, it is evident that G3 and G4 significantly contributed to these modes. Hence, we only focus on these two modes.

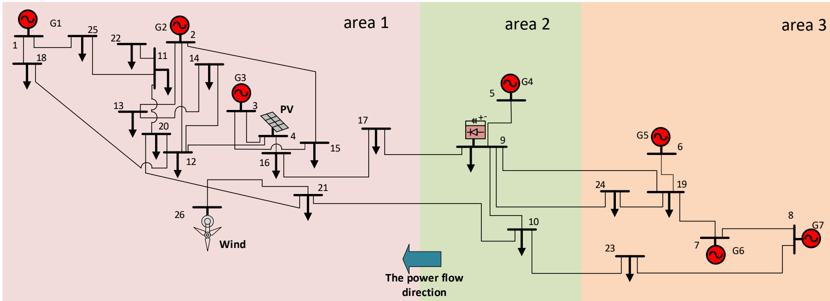

Figure 4. Java, Indonesia power grid representative model.

Table 1. Damping performance of Java, Indonesia grid.

Mode	Damping	Generator Participation
Interarea	0.00207	G3, G4
Local 1	0.00907	G6
Local 2	0.00211	G4
Local 3	0.00626	G1
Local 4	0.00625	G2
Local 5	0.2684	G7, G8
Local 6	0.1809	G8, G7

To investigate the performance of the system with the proposed control method, four different scenarios were considered, illustrated in Table 2. First, modal analyses and time-domain simulations were performed. Then, the comparison of damping performance in four different scenarios is reported. Moreover, nonlinear time-domain simulations were carried out to validate the results, and the resiliency of the controller was investigated. Different operating conditions were applied to the system to determine the resiliency of the controller. Lastly, the maximal RES penetration level for the Indonesian grid from the oscillatory stability point of view was estimated.

Table 2. Scenarios for simulation studies.

Scenario	Remarks
1	Modified Java system (Java system with PV, wind, and BESS)
2	Modified Java system with conventional wide-area POD located at wind, PV, and BESS
3	Modified Java system with resilient wide-area MMC located at wind, PV, and BESS
4	Modified system with resilient wide-area MMC using FA at BESS, PV, and wind

4.1. Numerical Results

This section focuses on the modal analysis of the Java, Indonesia power grid with the underlined scenarios, and it is given in Table 2. This analysis can be conducted by investigating the damping ratio of the targeted EM modes. In this paper, only local mode 2 and interarea mode were investigated since they were identified as critical modes in the Indonesian grid by the initial simulation studies. Figure 5 illustrates the damping ratio comparison under different scenarios. It is evident that the best damping performance was observed in Scenario 4. This could have happened because BESS, wind, and PV produce appropriate active and reactive power to the grid with the proposed MMC. To validate damping performance analysis, time-domain simulations were carried out. To observe the oscillatory condition of the system, a small disturbance was produced in the system by giving a 0.01 step input to the load. Figure 6 shows the rotor speed responses of G3 for various scenarios, while the rotor angle responses of G3 are given in Figure 7. In addition, Figure 8 shows the rotor speed response of G4, and Figure 9 shows the rotor angle response of G4. Rotor speed oscillation of G3 settled at 6 s with the proposed control, while the rotor speed oscillation of G4 settled at 7.5 s with the proposed controller. Figures 6 and 8 results show that the rotor speed oscillations of G3 and G4 took longer for Scenarios 1–3 than for Scenario 4. Similar trends could be observed for the rotor angle responses of G3 and G4 with the proposed MMC. Some deviations from the initial condition were observed due to the absence of the governor system in the synchronous generators.

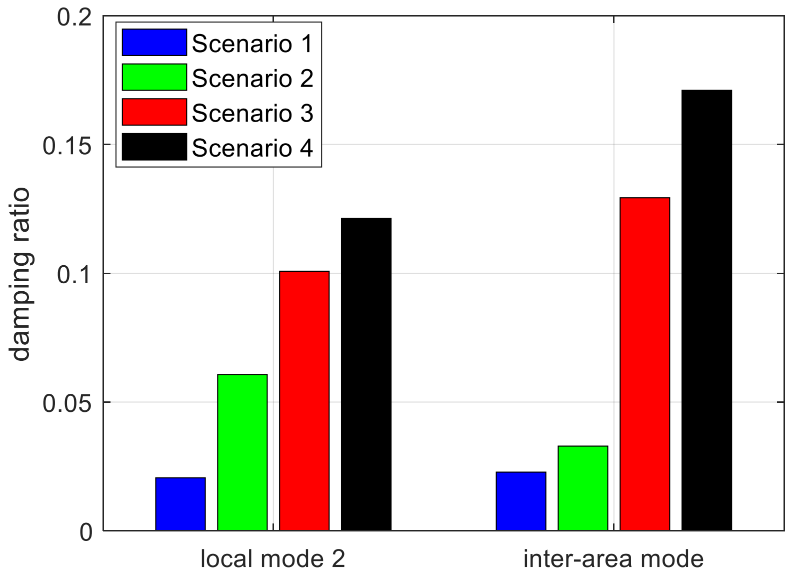

Figure 5. Damping performance comparison under different scenarios.

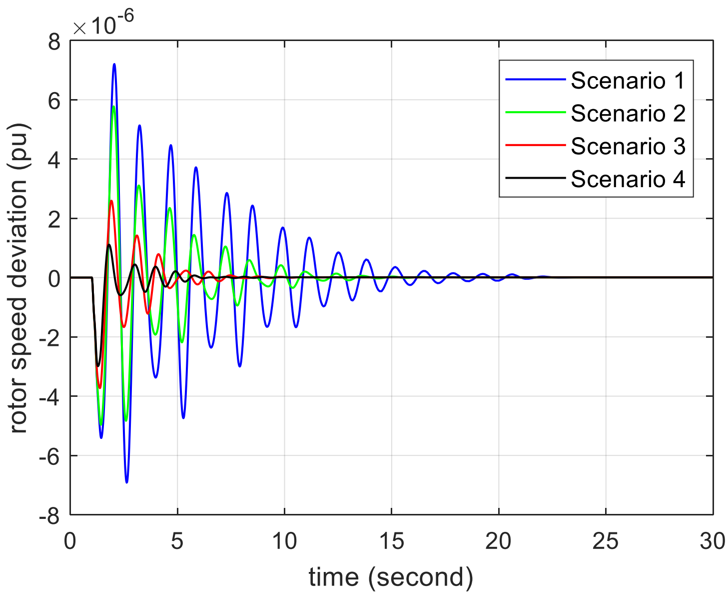

Figure 6. Rotor speed responses of G3.

For further investigation, the system was tested against large disturbances. These tests were carried out by applying a three-phase fault in the transmission line between Areas 1 and 2. Figures 10 and 11 depict the rotor speed responses of G3 and G4, respectively. Figures 10 and 11 results show that the rotor speed oscillations of G3 and G4 settled at approximately 10 s when using the proposed control scheme (i.e., Scenario 4). In the large disturbance situation, the proposed method (Scenario 4) was still superior to the other scenarios, as stated in Table 2.

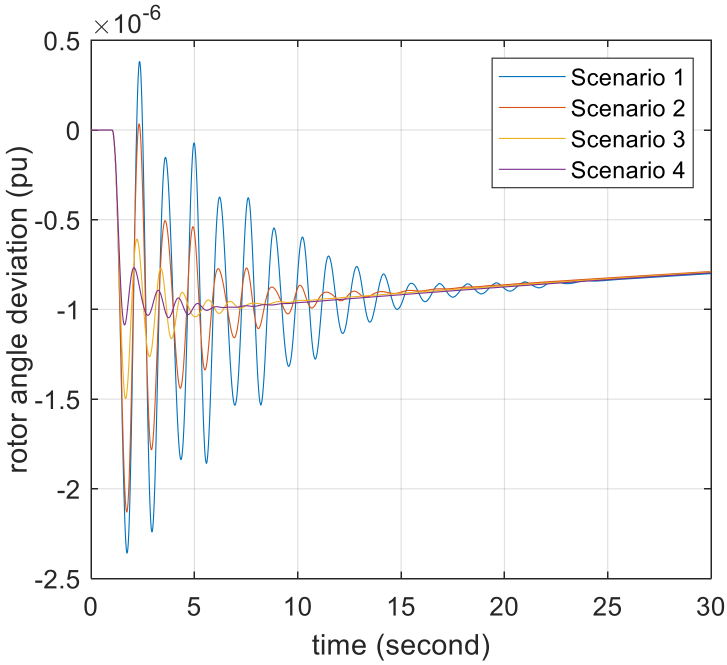

Figure 7. Rotor angle responses of G3.

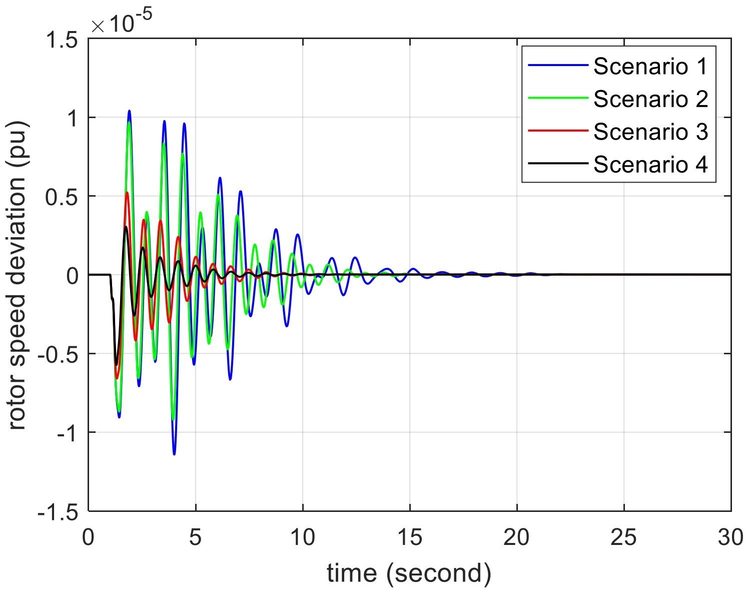

Figure 8. Rotor speed responses of G4.

Time-domain simulations were carried out to investigate the impact of the added MMC on the internal dynamics of wind, PV, and BESS. Similar to previous simulations, a three-phase fault was applied between Areas 1 and 2 to simulate large disturbance scenarios. Figure 12 shows the q-axis current response of the wind power system. Scenario 4 responses had greater magnitude compared to that of other scenarios. Similar to the wind power system, the q-axis current of the PV power system also had greater magnitude in Scenario 4, as shown in Figure 13. In addition, the d-axis current of BESS produced a similar result as those of ind and PV. As depicted in Figure 14, BESS's d-axis current in Scenario 4 had greater magnitude than that in other scenarios. This shows that the controller could modulate the output of wind, PV, and BESS so that they provided the higher output (within the limit) to dampen the oscillation of the system. Results showed that the proposed control did not adversely impact the internal dynamics of the RESs and BESS.

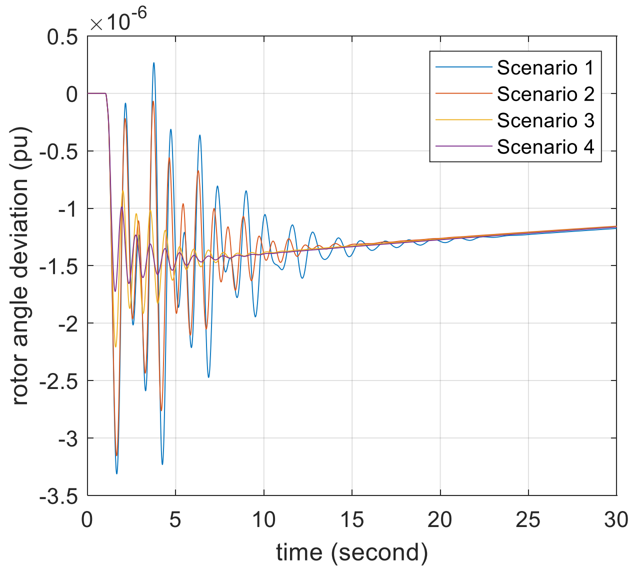

Figure 9. Rotor angle responses of G4.

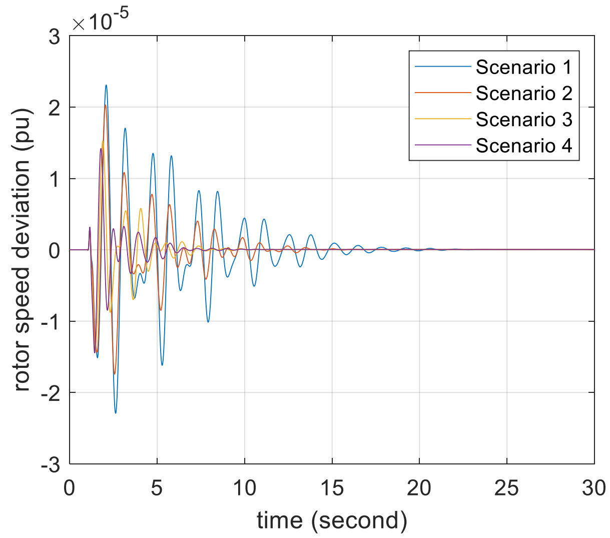

Figure 10. Rotor speed responses of G3.

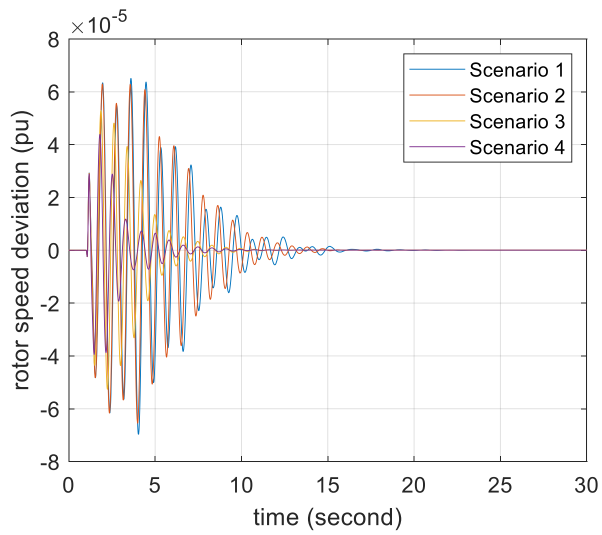

Figure 11. Rotor speed responses of G4.

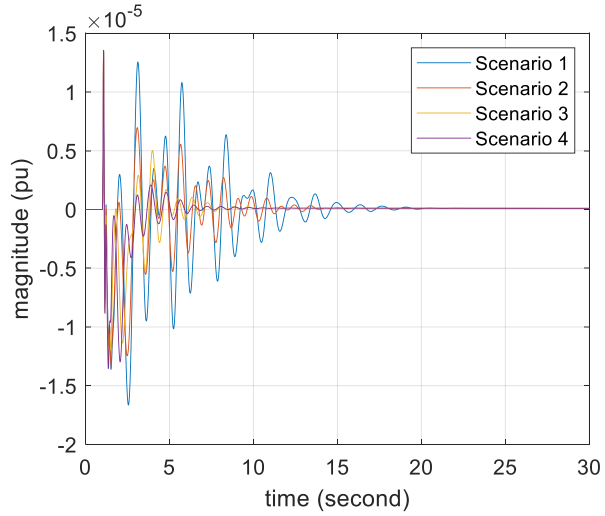

Figure 12. Q-axis current responses of wind generation.

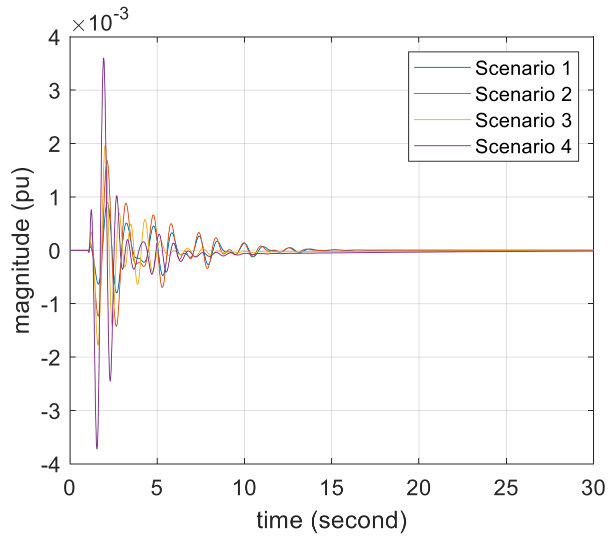

Figure 13. q-axis current response of the PV power system.

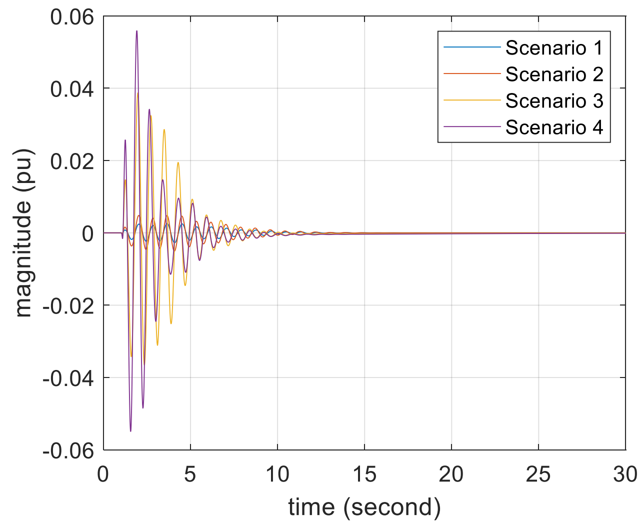

Figure 14. D-axis current responses of BESS.

4.2. Resilience Test

As shown in Figures 6–14, the proposed controller was superior compared to other controllers. Hence, in this section, the tested resiliency of the controller is reported. The resiliency of the controller was tested by disabling the wide-area signal. Moreover, the resiliency of the controller was tested by disabling one of the controllers in the proposed MMC structure.

Table 3 depicts the damping fluctuations of the critical mode resulting from the resiliency test. The damping ratio of local mode 2 and the interarea mode decreased when the communication and controllers were disabled. The worst condition was under controller failures occurring simultaneously at the wind and BESS locations. However, damping performance was better than the threshold value used in the utility (i.e., 0.05 pu), even in the worst-case scenario. Table 3 shows that the system experienced the lowest damping margin for the simultaneous outage of the controls in wind and BESS.

Table 3. Resilient test results.

Case	Local 2	Interarea
Normal condition	0.1710	0.1213
Loss of signals	0.1685	0.0775
BESS controller fail	0.1181	0.0629
WPS controller fail	0.0846	0.0631
PV controller fail	0.1284	0.0649
WECS and PV controller fail	0.0631	0.0635
PV and BESS controller fail	0.0866	0.0624
WECS and BESS controller fail	0.0563	0.0571

Figure 15 illustrates the rotor speed responses under loss of control signals, while Figure 16 shows the rotor speed responses of G3 and G4 under WECS (i.e., wind) and BESS controller failures. Higher rotor oscillations were observed for controller failure than for the loss of control signal. However, oscillations settled down within 15 s.

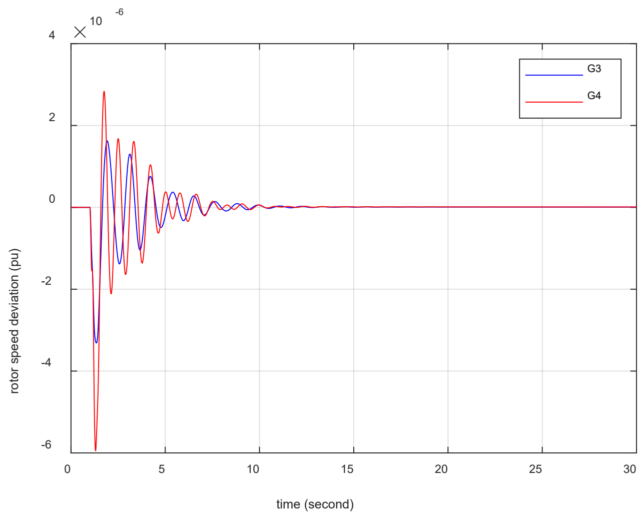

Figure 15. Rotor speed responses under loss of signal condition.

4.3. Impact of Increased RES Penetrations

The impact of penetration levels of RESs on the power system's oscillatory stability was investigated next. The penetration levels of RESs varied from 6% to 50% of the total system generation. The damping ratio was used to estimate how many RESs can be integrated into the Javan power system from a small-signal stability point of view. Tables 4 and 5 illustrate the comparison of the damping of interarea and local mode 2 variation due to the increasing penetration of RESs under different scenarios.

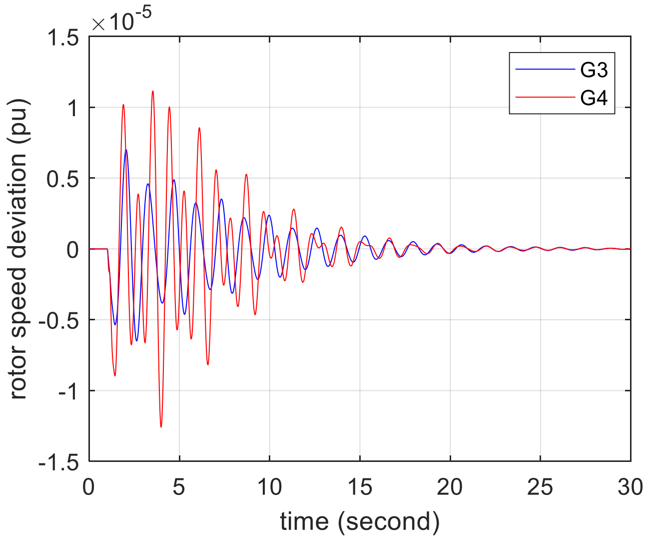

Figure 16. Rotor speed responses under WECS and BESS controller failure.

Table 4. Damping performance of interarea mode with high RESs.

Case	Scenario 2	Scenario 3	Scenario 4
6%	3.29	10.08	12.13
10%	3.12	9.13	11.74
20%	2.78	7.77	11.05
30%	1.91	5.35	9.34
40%	−1.79	3.12	5.81
50%	−2.12	2.11	5.00

Table 5. Damping performance of local mode 2 with high RESs.

Case	Scenario 2	Scenario 3	Scenario 4
6%	3.29	10.08	12.13
10%	3.12	9.13	11.74
20%	2.78	7.77	11.05
30%	1.91	5.35	9.34
40%	−1.79	3.12	5.81
50%	−2.12	2.11	5.00

Tables 4 and 5 show that the damping of the interarea mode was reduced with the increase in RE penetration. This happened due to the following reasons:

- lower total inertia of the system;
- change in the penetration direction;
- dynamic interactions and fast control of RESs.

The percentage damping of the interarea mode became negative for Scenario 2 under 35% and more penetration of RESs. The damping of interarea mode for Scenario 2 was also below the industry threshold, even when the penetration of RESs was at 6%. Furthermore, the damping margin of Scenario 3 was less than the minimal standard when RE penetration reached 30% and beyond. Moreover, for Scenario 4, the damping margin reached the threshold value under 50% penetration. It is also observed that the damping ratio of local mode 2 remains positive under 50% RES penetration for scenario 3. However, the damping value falls under the industry threshold when RESs are increased beyond 25%. Furthermore, the damping ratio of local mode 2 was higher than the threshold value, even beyond 50% RES penetration for Scenario 4. All EM modes damping should be over the threshold value for the small-signal stability secure operation of the power system. Therefore, Scenario 4 is only suitable for future Java, Indonesia power systems.

4.4. Comparison with Other Methods

The proposed metaheuristic method (Scenario 4) is compared with other well-known metaheuristic methods (particle swarm optimisation, sine cosine algorithm, grey wolf optimiser, and bat algorithm) to assess its effectiveness. Figure 17 compares the execution time between the proposed metaheuristic method compared with particle swarm optimisation (PSO), sine cosine algorithm (SCA), grey wolf optimiser (GWO), and bat algorithm (BA). The proposed method's execution time was faster (e.g., 7.6 min) than that of other methods. From the given results, it is evident that the execution time of the well-known PSO method was almost three times faster than that of the FA method. If the size and complexity of the system increase, the execution time is also expected to increase. It is thus recommended to use the algorithm with shorter execution time and high accuracy.

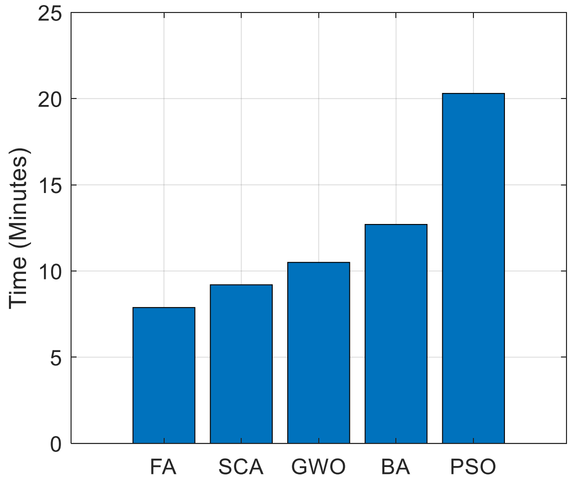

Figure 17. Comparison of execution time.

The ranking index given in [33] was used to assess the performance of the proposed controller. Three different ranking indices were used for the comparison: performance, robustness, and simplicity ranks. The mathematical representations of this controller's performance ranking are described below. Controller performance was assessed on the basis of the index given in (31) [25].

$$
\begin{aligned}
I_{Performance} = w^{\zeta} N\left[\zeta^{POD} - \zeta^{base}\right] + w^{t} N\left[\tau^{POD} - \tau^{base}\right] + \\
w^{\Delta\delta} N\left[\Delta\delta^{POD} - \Delta\delta^{base}\right]
\end{aligned}
\tag{31}
$$

Controller robustness is assessed by evaluating how system performance varies with operating conditions. The robustness ranking index used in this work can be expressed as (32) [25].

$$
I_{Robust} = w^{all} N\left[\frac{1}{M}\sum_{i=1}^{M}\left(\zeta^{POD} - \zeta^{base}\right)\right] + w^{min[\zeta_{min}^{PODbase_{min}}]}
\tag{32}
$$

The POD controller tuning time is used to assess the simplicity associated with various POD designs. The simplicity ranking score can be determined by (33) [33].

$$
I_{Simplicity} = w^{t} N\left[\left(t^{POD}\right)^{-1}\right] + w^{c} N\left[\left(n^{code}\right)^{-1}\right] + w^{p} N\left[p^{POD}\right]
\tag{33}
$$

Figure 18 illustrates the controller performance rank comparison between the proposed metaheuristic method and other metaheuristic methods.

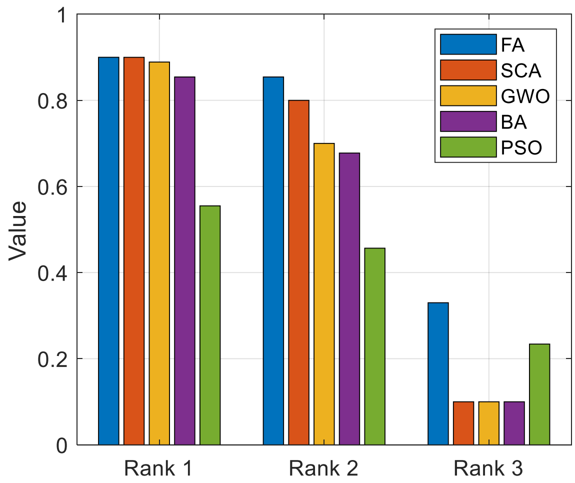

Figure 18. Controllers ranking indexes.

Figure 16 shows the superior performance of the proposed metaheuristic method over the PSO, BA, SCA, and GWO in all three ranking indices. However, all methods do not provide satisfactory results in the simplicity ranking.

5. Conclusions

This paper proposed a firefly-algorithm-based resilient wide-area multimodal controller (MMC) for power systems with large BESS, wind, and PV integration. The performance of the proposed approach was assessed using a modified version of the Java, Indonesia power system. The considered case studies confirmed the ability of the proposed resilient wide-area MMC to maintain satisfactory damping ratios even under severe communication and controller failures, and in the presence of various renewable energy penetration levels. The outage of two consecutive controllers had a significant effect on the damping performance of the system. From the results, it is evident that some critical control loops in the MMC had higher impact on the system damping margin due to the controllability and observability of the loop. Additionally, the proposed controller had no adverse effects on the internal dynamics of the wind, PV, and BESS systems, as shown by the nonlinear time-domain responses of wind, PV, and BESS. The proposed multimodal controller can enhance the penetration of renewable energy penetration in the Java power system by up to 50%. Moreover, FA achieved better performance compared with that of the other algorithms in this paper. In terms of execution time, FA could find the MMC parameters in around 7 min, while the other algorithms required more than 10 min. Further research can be conducted by designing an adaptive MMC on the basis of an extreme learning machine to handle the uncertainty of a renewable power plant.

Author Contributions: Conceptualisation, H.S., N.M., R.S. and M.R.I.; methodology, H.S., N.M., M.R.I., A.F. and M.A.; validation, H.S., R.S. and M.R.I.; formal analysis, H.S., N.M. and M.R.I.; investigation, H.S. and M.A.; resources, H.S., A.F. and A.U.K.; writing—original draft preparation, H.S. and A.U.K.; writing—review and editing, R.S., N.M. and M.R.I.; visualisation, H.S., M.A. and M.R.I. All authors have read and agreed to the published version of the manuscript.

Funding: This research received no external funding.

Institutional Review Board Statement: Not applicable.

Data Availability Statement: Not applicable.

Conflicts of Interest: The authors declare no conflict of interest.

Appendix A

Table A1. Optimal control parameters.

Index	Value
KΔω	5 pu
KΔpe	1.462 pu
T1	0.05 s
T2	0.02 s
T3	0.03 s
T4	0.01 s
Tw2	10 s
Tw3	10 s

Algorithm A1: Firefly algorithm pseudocode.

1. Initialize parameter: iteration, γ, β, α, D, n
   /* α value varies between 0 to 1*/
   /* D is the dimension of the solution*/
   /* γ value varies between 0 to 1*/
   /* β value varies between 0 to 1*/
   /* n is number of fireflies*/
2. Initialize random population:
   $$x = rand();$$
3. Initial population evaluation using the objective function:
   $$Objective = min(aZ_1 + bZ_2 + cZ_3)$$
4. Define intensity at cost (x) of each individual
5. While iteration < iteration:
6. For each i = 1 to n
7. For each j = 1 to n
8. If (intensity > intensity)
9. Move firefly i to j in particular dimension
10. End if
11. Evaluate new solution and updating the light intensity
12. End for j
13. End for i
14. Rank the fireflies and find the current best value
15. End while
16. Print the results
17. End firefly algorithm process

References

1. Markovic, U.; Stanojev, O.; Aristidou, P.; Vrettos, E.; Callaway, D.S.; Hug, G. Understanding small-signal stability of low-inertia systems. *IEEE Trans. Power Syst.* **2021**, *36*, 3997–4017. [CrossRef]
2. Pan, Y.; Liu, F.; Chen, L.; Wang, J.; Qiu, F.; Shen, C.; Mei, S. Towards the Robust Small-Signal Stability Region of Power Systems Under Perturbations Such as Uncertain and Volatile Wind Generation. *IEEE Trans. Power Syst.* **2018**, *33*, 1790–1799. [CrossRef]
3. Yorino, N.; Abdillah, M.; Sasaki, Y.; Zoka, Y. Robust power system security assessment under uncertainties using bi-level optimization. *IEEE Trans. Power Syst.* **2017**, *33*, 352–362. [CrossRef]
4. El-Shimy, M.; Sharaf, A.; Khairy, H.; Hashem, G. Reduced-order modelling of solar-PV generators for small-signal stability assessment of power systems and estimation of maximum penetration levels. *IET Gener. Transm. Distrib.* **2018**, *12*, 1838–1847. [CrossRef]
5. Gautam, D.; Vittal, V.; Harbour, T. Impact of Increased Penetration of DFIG-Based Wind Turbine Generators on Transient and Small Signal Stability of Power Systems. *IEEE Trans. Power Syst.* **2009**, *24*, 1426–1434. [CrossRef]
6. Bian, X.Y.; Geng, Y.; Lo, K.L.; Fu, Y.; Zhou, Q.B. Coordination of PSSs and SVC Damping Controller to Improve Probabilistic Small-Signal Stability of Power System with Wind Farm Integration. *IEEE Trans. Power Syst.* **2016**, *31*, 2371–2382. [CrossRef]
7. Zhou, Y.; Li, Y.; Liu, W.; Yu, D.; Li, Z.; Liu, J. The stochastic response surface method for small-signal stability study of power system with probabilistic uncertainties in correlated photovoltaic and loads. *IEEE Trans. Power Syst.* **2017**, *32*, 4551–4559. [CrossRef]

8. Peres, W. Multi-band power oscillation damping controller for power system supported by static VAR compensator. *Electr. Eng.* **2019**, *101*, 943–967. [CrossRef]
9. Dasu, B.; Kumar, M.S.; Rao, R.S. Design of robust modified power system stabilizer for dynamic stability improvement using Particle Swarm Optimization technique. *Ain Shams Eng. J.* **2019**, *10*, 769–783. [CrossRef]
10. Peres, W.; Coelho, F.C.R.; Costa, J.N.N. A pole placement approach for multi-band power system stabilizer tuning. *Int. Trans. Electr. Energy Syst.* **2020**, *30*, 12548. [CrossRef]
11. Gurung, S.; Naetiladdanon, S.; Sangswang, A. Coordination of power-system stabilizers and battery energy-storage system controllers to improve probabilistic small-signal stability considering integration of renewable energy resources. *Appl. Sci.* **2019**, *9*, 1109. [CrossRef]
12. Alias, F.; Singh, M. Damping sensitivity analysis and optimized battery controller for small-signal stability enhancement in wind penetrated networks. *Sustain. Energy Grids Netw.* **2021**, *26*, 100441. [CrossRef]
13. Ahmed, M.; Vahidnia, A.; Datta, M.; Meegahapola, L. An adaptive power oscillation damping controller for a hybrid AC/DC microgrid. *IEEE Access* **2020**, *8*, 69482–69495. [CrossRef]
14. Setiadi, H.; Mithulananthan, N.; Shah, R.; Raghunathan, T.; Jayabarathi, T. Enabling resilient wide-area POD at BESS in Java, Indonesia 500 kV power grid. *IET Gener. Transm. Distrib.* **2019**, *13*, 3734–3744. [CrossRef]
15. Setiadi, H.; Mithulananthan, N.; Shah, R.; Lee, K.Y.; Krismanto, A.U. Resilient wide-area multi-mode controller design based on Bat algorithm for power systems with renewable power generation and battery energy storage systems. *IET Gener. Transm. Distrib.* **2019**, *13*, 1884–1894. [CrossRef]
16. Dey, N. *Applications of Firefly Algorithm and Its Variants*; Springer: Singapore, 2020.
17. Singh, M.; Patel, R.N.; Neema, D.D. Robust tuning of excitation controller for stability enhancement using multi-objective metaheuristic Firefly algorithm. *Swarm Evol. Comput.* **2019**, *44*, 136–147. [CrossRef]
18. Naderipour, A.; Abdul-Malek, Z.; Ramachandaramurthy, V.K.; Miveh, M.R.; Moghaddam, M.J.H.; Guerrero, J. Optimal SSSC-based power damping inter-area oscillations using firefly and harmony search algorithms. *Sci. Rep.* **2020**, *10*, 12176. [CrossRef]
19. Ravindrababu, M.; Saraswathi, G.; Sudha, K.R. Design of UPFC-PSS using Firefly Algorithm for Stability Improvement of Multi-Machine System under Contingency. *J. Electr. Eng.* **2019**, *13*, 21–39.
20. Zou, Y.; He, J. Comprehensive modeling, simulation and experimental validation of Permanent Magnet Synchronous generator wind power system. In Proceedings of the 2016 IEEE/IAS 52nd Industrial and Commercial Power Systems Technical Conference (I&CPS), Detroit, MI, USA, 1–5 May 2016; pp. 1–9.
21. Yin, M.; Li, G.; Zhou, M.; Zhao, C. Modeling of the Wind Turbine with a Permanent Magnet Synchronous Generator for Integration. In Proceedings of the 2007 IEEE Power Engineering Society General Meeting, Tampa, FL, USA, 24–28 June 2007; pp. 1–6.
22. Krismanto, A.U.; Sulistiawati, I.B.; Limpraptono, F.Y.; Priyadi, A.; Setiadi, H.; Abdillah, M. Impact of Large-Scale Wind Power Penetration on Dynamic Voltage Stability of Interconnected Power System: An Indonesia Case Study. *Int. J. Intell. Eng. Syst.* **2021**, *14*, 251–263. [CrossRef]
23. Shah, R.; Mithulananthan, N.; Lee, K.Y. Large-scale PV plant with a robust controller considering power oscillation damping. *IEEE Trans. Energy Convers.* **2012**, *28*, 106–116. [CrossRef]
24. *WECC Solar Plant Dynamic Modeling Guidelines*; WECC: Salt Lake City, UT, USA, 2014.
25. Elliott, R.T.; Ellis, A.; Pourbeik, P.; Sanchez-Gasca, J.J.; Senthil, J.; Weber, J. Generic photovoltaic system models for WECC-A status report. In Proceedings of the 2015 IEEE Power & Energy Society General Meeting, Denver, CO, USA, 26–30 July 2015; pp. 1–5.
26. Clark, K.; Miller, N.W.; Walling, R. *Modeling of GE Solar Photovoltaic Plants for Grid Studies*; General Electric International. Inc.: Schenectady, NY, USA, 2010; p. 12345.
27. Chandra, S.; Gayme, D.F.; Chakrabortty, A. Coordinating wind farms and battery management systems for inter-area oscillation damping: A frequency-domain approach. *IEEE Trans. Power Syst.* **2013**, *29*, 1454–1462. [CrossRef]
28. Kerdphol, T.; Fuji, K.; Mitani, Y.; Watanabe, Y.; Qudaih, Y. Optimization of a battery energy storage system using particle swarm optimization for stand-alone microgrids. *Int. J. Electr. Power Energy Syst.* **2016**, *81*, 32–39. [CrossRef]
29. Shakarami, M.R.; Davoudkhani, I.F. Wide-area power system stabilizer design based on Grey Wolf Optimization algorithm considering the time delay. *Electr. Power Syst. Res.* **2016**, *133*, 149–159. [CrossRef]
30. Yang, X.-S. *Nature-Inspired Metaheuristic Algorithms*; Luniver Press: Somerset, UK, 2010.
31. Yang, X.-S. Metaheuristic optimization. *Scholarpedia* **2011**, *6*, 11472. [CrossRef]
32. *Peraturan Pemerintah Republik Indonesi No. 79 Tahun 2014 Tentang Kebijakan Energi Nasional*; Peraturan Pemerintah Republik Indonesi: Jakarta, Indonesia, 2014.
33. Zhang, Y.; Preece, R. A comprehensive methodology for assessing power oscillation damping controllers for HVDC-based system stabilization. In Proceedings of the 2015 IEEE Eindhoven PowerTech, Eindhoven, The Netherlands, 29 June–2 July 2015; pp. 1–6.